Physics of Contrast-Enhanced Mammography

2

Cécile R. L. P. N. Jeukens

2.1 Image Formation in Mammography

To acquire a mammogram, the breast is compressed by a paddle to make the breast uniform in thickness and to minimize superimposition of fibroglandular tissue, which could mimic breast lesions. X-rays produced in the X-ray tube of the mammography unit are directed to the breast below which the detector is located (Fig. 2.1).

2.1.1 Generation of X-Rays

In the X-ray tube, the X-rays are generated as follows (Fig. 2.2a). The cathode is heated by the tube current, resulting in the release of electrons. The electrons are accelerated toward the anode by the tube voltage and hit the anode, also called the target. In the anode, the electrons interact with nuclei of the anode material, and bremsstrahlung is released, which in fact is the X-ray radiation used for imaging (Fig. 2.2b). The energy of the photons depends on the strength of the interaction: the closer the electron approaches the nucleus, the stronger the interaction becomes. The interaction strength varies per electron hitting the anode, and consequently the X-ray photons have many different energies resulting in an X-ray spectrum rather than a single photon energy. The maximum energy is determined by the maximal acceleration of the electrons which is dictated by the tube voltage. By adding a filter in the X-ray beam, the low-energy X-ray photons are absorbed. This is beneficial for the dose to the breast as the low-energy photons are so strongly attenuated in the breast that they are completely absorbed in the breast before reaching the detector.

C. R. L. P. N. Jeukens (✉)
Department of Radiology and Nuclear Medicine, Maastricht University Medical Center, Maastricht, The Netherlands
e-mail: cecile.jeukens@mumc.nl

M. Lobbes, M. S. Jochelson (eds.), *Contrast-Enhanced Mammography*,
https://doi.org/10.1007/978-3-030-11063-5_2

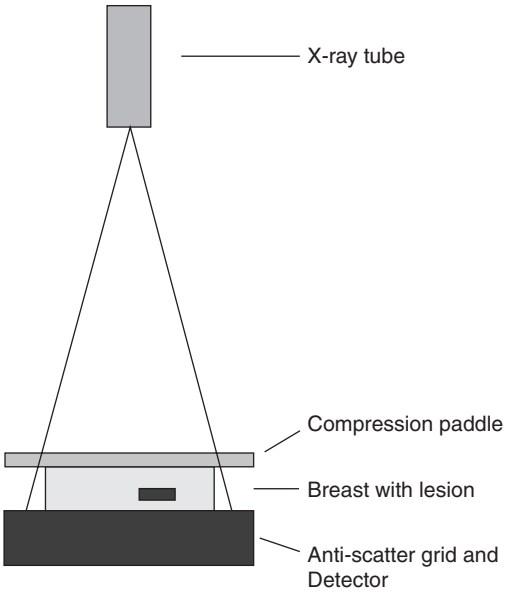

Fig. 2.1 Schematic set-up of a mammography system

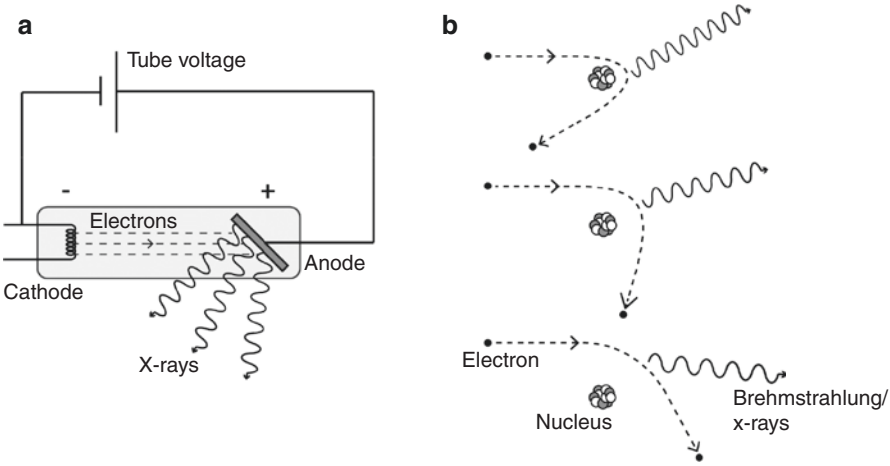

Fig. 2.2 (**a**) Schematic of an X-ray tube showing the cathode where the electrons are released and attracted towards the positively charged anode. X-rays are generated in the anode during the interaction of electrons with the nuclei of the anode atoms. The cathode and anode are positioned in a vacuum indicated by the grey shaded area. (**b**) Depending on the distance the electron approaches the nucleus a stronger or less strong interaction takes place resulting in higher and lower energy photons. This is the reason that an X-ray tube emits a multi-energetic spectrum of photons

As such, these low-energy photons do not contribute to image formation, while they do contribute to the radiation dose of the breast. The final X-ray spectrum is determined by the combination of tube voltage, anode material, and filter material.

2.1.2 Attenuation of X-Rays in the Breast

In the breast the X-rays are partly absorbed and partly transmitted. The transmitted X-rays reach the detector to form the image. The challenge is to visualize both benign and malignant breast structures. Differences between attenuation properties of the glandular, adipose, and cancerous tissue lead to image contrast. The attenuation of tissue (or any material in fact) is characterized by the linear attenuation coefficient indicated by the symbol μ, which describes how much the tissue attenuates radiation per cm of tissue. The value of the attenuation coefficient depends on the type of tissue and the energy of the X-ray radiation.

The attenuation properties of glandular, adipose, and cancerous tissue are comparable (Fig. 2.3). This makes it challenging to achieve sufficient contrast in mammographic images. For lower photon energies, the differences between the attenuation coefficient of the different tissues increase leading to improved contrast between these tissues [5]. This is the reason for using very low tube voltages (range 25–34 kV) in mammography when compared to other radiological applications (typically 50–140 kV). However, for low photon energies, increasing attenuation results in increasing photon absorption in the breast, decreasing the number of photons reaching the detector and noisier images while increasing the dose to the breast. The choice of the most ideal X-ray spectrum is therefore a trade-off. With modern full-field digital mammography (FFDM) units employing low-energy X-ray spectra (kVp ~25–34 kV, with additional filtration), advanced digital detectors, anti-scatter grids, proper breast compression, and advanced post-processing algorithms, high-quality diagnostic images can be obtained with low dose to the breasts.

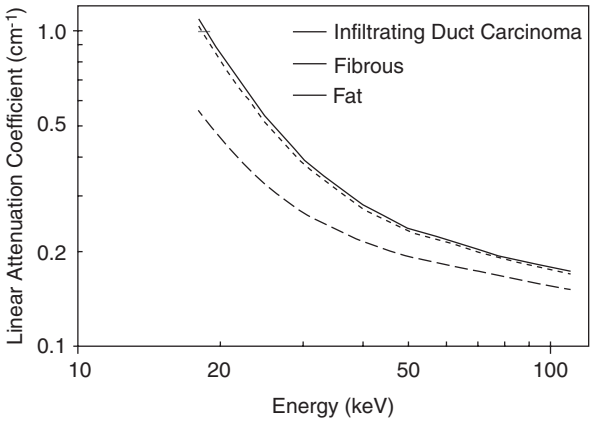

Fig. 2.3 Linear attenuation coefficient as a function of energy for adipose and glandular breast tissue and infiltrating ductal carcinoma [5]. The attenuation of the carcinoma and glandular tissue is very similar making it difficult to obtain sufficient contrast. Image is based on data published in ref. [5]

2.2 Enhancement by Iodine Contrast Agent

Iodinated contrast enhances the contrast between malignant lesions and normal breast tissue enabling improved breast cancer detection: When tumors grow, they develop blood vessels to provide nutrients and oxygen to the tumor in a process called "angiogenesis." These new blood vessels are rapidly formed and therefore "leaky," which allows contrast agent to extravasate from these vessels into the tumor itself, causing it to enhance when dedicated imaging protocols are used [6]. The attenuation coefficient μ of the iodine shows a discontinuity called the *k*-edge at an energy level of 33.2 keV, while the attenuation coefficient μ of the breast tissue continues to gradually decrease (Fig. 2.4). These differences in attenuation between the iodine contrast agent containing breast lesion and the surrounding breast tissue are exploited in dual-energy mammography to visualize the iodine contrast enhancement.

2.2.1 The *k*-Edge of Iodine

The X-ray radiation is absorbed in the iodinated contrast agent primarily by the photoelectric effect. This is a process in which an X-ray photon interacts with the innermost electron shells of the iodine atom (Fig. 2.5). The incoming X-ray photon is completely absorbed, and an electron is ejected from the atom. Depending on its energy, the X-ray photon interacts with the first (K), second (L), third (M), etc. electron shell. A higher energy is required for the lower, innermost shells. The

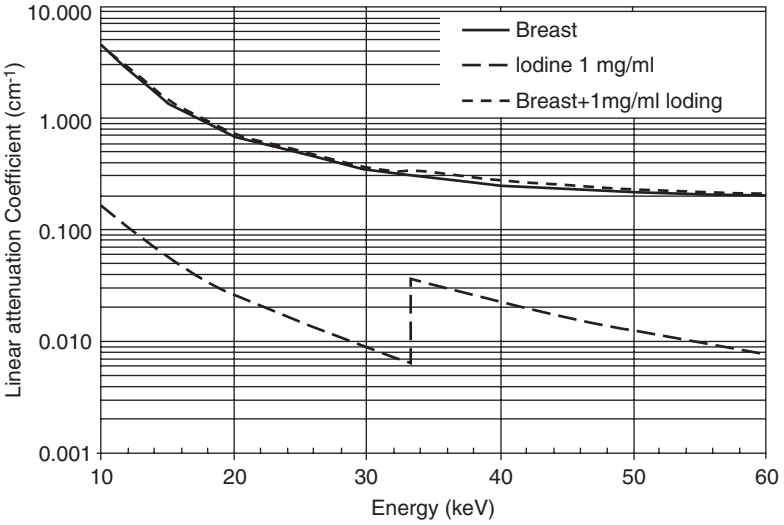

Fig. 2.4 Attenuation coefficient as a function of photon energy for breast tissue and 1 mg/ml iodine [7], where the latter shows a *k*-edge at 33.2 keV. Note the logarithmic scale on the *y*-axis. To appreciate the small contribution of the iodine to the total attenuation the sum of the breast and 1 mg/ml iodine attenuation is shown

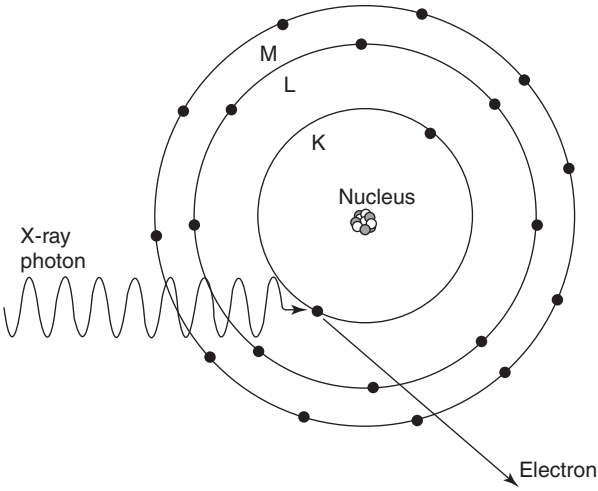

Fig. 2.5 Illustration of the photoeffect: an X-ray photon interacts with an electron from the inner shells. The energy of the photon is completely absorbed and the electron is ejected from the atom

probability that the X-ray photons are absorbed decreases with increasing photon energy. However, when the photon energy is high enough to match the energy required for ejecting an electron from the innermost shell, the so-called K-shell, the X-ray photon absorption probability suddenly increases (about five times for iodine [7], Fig. 2.4), after which it gradually decreases again with increasing photon energy. This sudden increase is called the *k*-edge, and the energy value at which it occurs is specific for the atom with which the incoming photon interacts. For iodine, the *k*-edge is at 33.2 keV. In analogy, also a L- and M-edge occurs, but for iodine these are observed at much lower photon energies to be clinically relevant.

2.2.2 Visualizing Iodine in the Breast

Although the iodine has a much higher attenuation coefficient per unit mass than the breast tissue, it is not visible in a regular mammogram because the iodine concentration in breast lesions is very low. For the standard injection protocol used in CEM (1.5 ml/kg body weight, iodine concentration: 300–350 mg/ml), the concentration in low to normal enhancing lesions is in the order of 1–4 mg/ml [8]. To illustrate, Fig. 2.4 also shows the sum of the breast and iodine attenuation where 1 mg/ml iodine leads to only a small increase of the total attenuation.

The iodine can be visualized by acquiring two images, taken with sufficiently different photon energies and subsequently performing post-processing on these images. Iodine shows a *k*-edge in the photon energy range used in mammography, and this sudden increase in absorption can be exploited to enhance differences between iodine-enhanced lesions and non-iodinated normal breast tissue. To this extent, it is important to choose the spectra of the two images properly: one with an X-ray spectrum below the *k*-edge of iodine and one with a spectrum above. These two CEM images are called low-energy and high-energy images, respectively.

2.2.3 Spectra of the Low-Energy and High-Energy Image

The X-ray spectrum of the low-energy image is equal to that of a FFDM image. Typically, a tube voltage of 25–34 kV is used, tungsten (W), rhodium (Rh), or molybdenum (Mo) as anode material and silver (Ag), Rh, or Mo as filter material. The low-energy image spectrum is below the *k*-edge of iodine (see, e.g., spectrum Fig. 2.6), and although iodine is present in the breast (as it is injected approximately 2 min prior to image acquisition), it is invisible on the low-energy image. Recent studies have shown that the low-energy CEM images are diagnostically equal to "regular" FFDM images [9–11].

For the high-energy image, the X-ray spectrum is generated with a higher tube voltage of 45–49 kV and a titanium (Ti) or copper (Cu) filter, with the same anode materials (see, e.g., Fig. 2.6). The filter is chosen to remove as many X-ray photons as possible with energies below the *k*-edge of iodine and to separate the high-energy spectrum from the low-energy spectrum.

2.2.4 Acquisition of CEM Images

To begin the CEM exam, patients are injected intravenously with a nonionic, monomeric, low-osmolar iodine contrast agent at a dose of 1.5 ml/kg of body weight. The most frequently used dose is 300 mg/ml iodine or more. The use of an automated injector is recommended (flow rate of 2–3 ml/s, followed by a saline bolus) using at least a 20 G needle. After an at least 2-min delay to allow the contrast agent to disperse in the breast, acquisition of mammographic images can commence ideally in

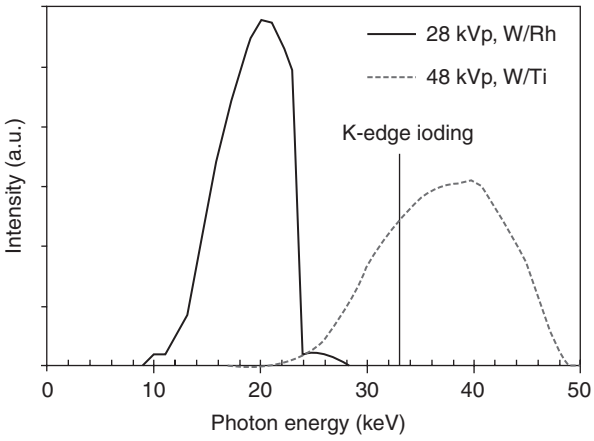

Fig. 2.6 Example of a low-energy (solid line) and high-energy (dotted line) spectrum used in clinical practice. The vertical line indicates the iodine *k*-edge at 33.2 keV showing that the low-energy spectrum is well below the kedge, while the high-energy spectrum is largly above. For visualization, the spectra are normalized to the same area under the curve. In practice the high-energy spectrum delivers a lower dose than the low-energy spectrum

the same order as is normally used in FFDM. The image acquisition usually takes 5–8 min postinjection which is well within the generally accepted time window of 10 min after contrast administration in which the image acquisition needs to be completed [12].

During each CEM acquisition, the low- and high-energy images are acquired directly after each other during the same breast compression: after the first acquisition, the mammography system rapidly switches the filter and the tube voltage to minimize the time between the two acquisitions. The total breast compression time of a single CEM exposure is typically 2–22 s, depending on the breast composition and thickness.

2.3 Post-processing to Obtain the Contrast-Enhanced (Recombined) Image

2.3.1 Concept of Post-processing

To obtain the contrast-enhanced image (also called the recombined image), the low- and high-energy images are processed using a weighted subtraction [13–16]. This involves three steps (Fig. 2.7). First, the images are log-transformed using the natural logarithm. The reason for this step is that X-ray radiation is exponentially attenuated when passing through the breast and the natural logarithm is the mathematical

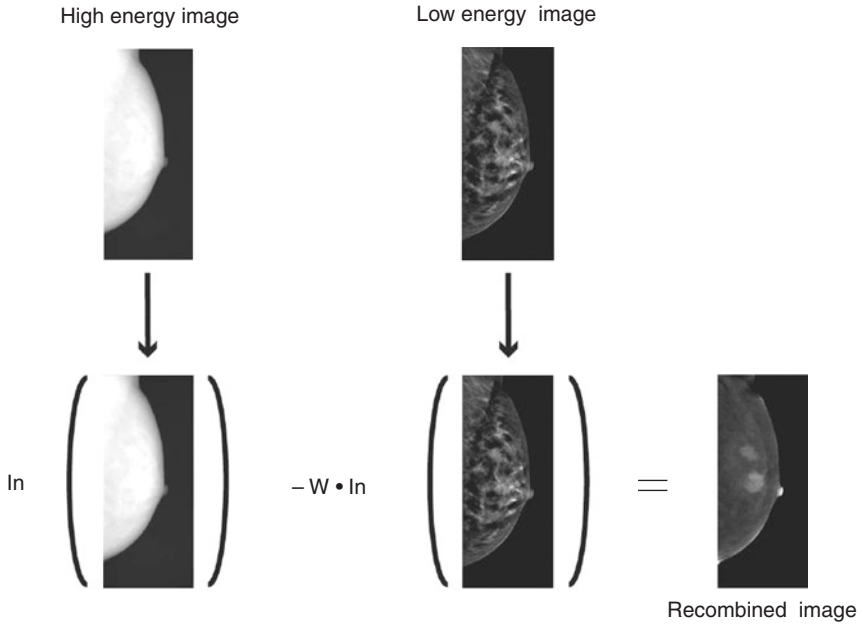

Fig. 2.7 Visual presentation of the postprocessing to obtain the contrast-enhanced recombined image from the low- and high-energy acquisition

counterpart of an exponential function. Second, the log-transformed low-energy image is multiplied by the weighting factor *w*, which is a number that depends on the low- and high-energy attenuation coefficients of normal breast tissue, which in turn depends on the used spectra. Finally, the weighted log-transformed low-energy image is subtracted from the log-transformed high-energy image. The resulting image, which shows areas of iodine accumulation or "enhancement," is called the recombined image.

It is important that in the second step the weighting factor *w* is chosen so that the normal tissue is canceled out, while the iodine contrast agent is not. In choosing the weighting factor, the *k*-edge of iodine is exploited. For the breast tissue, the attenuation coefficient gradually decreases for increasing photon energy (Fig. 2.4), while for the iodine a marked increase at the *k*-edge is present. These differences in attenuation coefficients between low- and high-energy for tissue and iodine allow to further enhance the iodine signal resulting in an image that is dominated by the iodine signal.

2.3.2 Mathematical Description of the Post-processing

For simplification, it is assumed that images are obtained with monoenergetic X-rays, i.e., not a poly-energetic X-ray spectrum as in clinical practice but a single X-ray energy. Although the attenuation coefficients of the glandular and adipose tissue are energy dependent (Fig. 2.3), they are also assumed to be represented by a single attenuation coefficient.

To explain the principle, the attenuation in the breast is considered in a single voxel (Fig. 2.8). The voxel is a 2D projection of a volume and contains a lesion with iodine contrast agent and normal breast tissue. The thickness of the lesion is denoted by *T*, and the thickness of the normal breast tissue is denoted by *t*, which equals the total compressed breast thickness (CBT) minus the lesion thickness. Both the lesion and the normal tissue absorb the X-rays. The absorption is given by an attenuation coefficient μ which is different for the lesion and the normal tissue. Moreover, the attenuation coefficient is different for the low- and high-energy X-rays. Four μ-values are involved: lesion low- and high-energy (denoted by $\mu_{\mathrm{l}}^{\mathrm{LE}}$ and $\mu_{\mathrm{l}}^{\mathrm{HE}}$, where l indicates lesion and LE and HE indicate low-energy and high-energy) and normal tissue low- and high-energy ($\mu_{\mathrm{t}}^{\mathrm{LE}}$ and $\mu_{\mathrm{t}}^{\mathrm{HE}}$, where t denotes tissue). The X-ray radiation is attenuated by the lesion and the normal tissue. How much attenuation takes place is determined by the attenuation coefficient of the material multiplied by the thickness: ($\mu_{\mathrm{t}}^{\mathrm{LE}} \cdot t + \mu_{\mathrm{l}}^{\mathrm{LE}} \cdot T$) and ($\mu_{\mathrm{t}}^{\mathrm{HE}} \cdot t + \mu_{\mathrm{l}}^{\mathrm{HE}} \cdot T$) for the low- and high-energy image, respectively. According to the Lambert-Beer law, the intensity of the incoming X-rays is attenuated exponentially when passing through the tissue and the lesion. The X-ray intensity reaching the detector can be described by the following equation:

$$I_{\mathrm{d}}^{\mathrm{LE}} = I_{0}^{\mathrm{LE}} \cdot \mathrm{e}^{-\left(\mu_{\mathrm{t}}^{\mathrm{LE}} \cdot t + \mu_{\mathrm{l}}^{\mathrm{LE}} \cdot T\right)} \quad \textit{and} \quad I_{\mathrm{d}}^{\mathrm{HE}} = I_{0}^{\mathrm{HE}} \cdot \mathrm{e}^{-\left(\mu_{\mathrm{t}}^{\mathrm{HE}} \cdot t + \mu_{\mathrm{l}}^{\mathrm{LE}} \cdot T\right)} \tag{2.1}$$

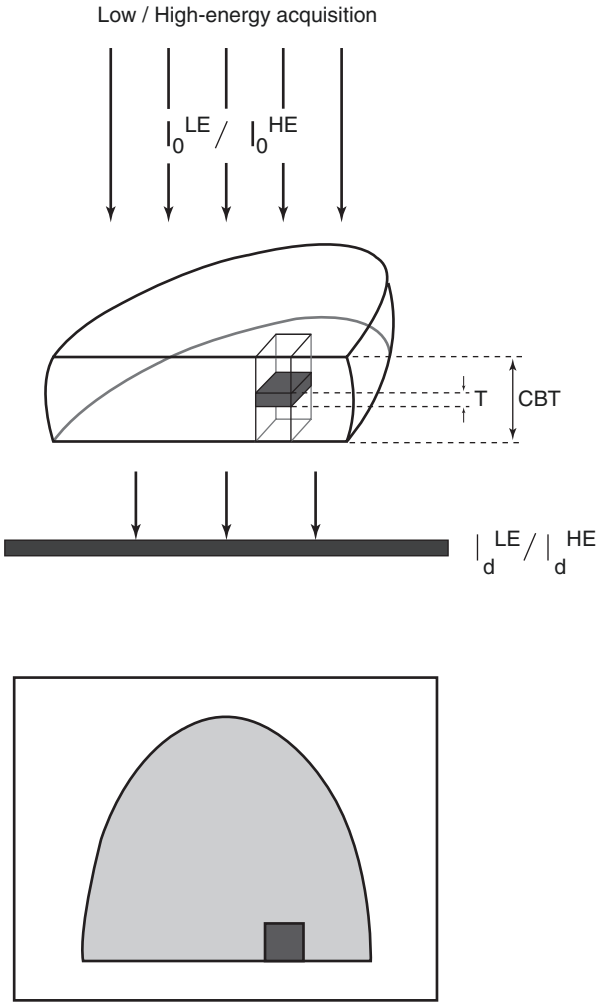

Fig. 2.8 Schematic representation of the breast for the mathematical description of the postprocessing. *I* indicates the intensity of the incoming (0) and transmitted (*d*) low- (LE) and high- (HE) energy X-rays, CBT is the total compressed breast thickness and *T* is the lesion thickness

where I_0^{LE} and I_0^{HE} are the intensities of the incoming X-rays for the low- and high-energy image, respectively; $I_{\mathrm{d}}^{\mathrm{LE}}$ and $I_{\mathrm{d}}^{\mathrm{HE}}$ are the intensities of the X-rays reaching the detector for the low- and high-energy image, respectively; μ denotes the attenuation coefficient; the sub- and superscripts are explained above; and T and t are the thickness of the lesion and normal tissue, respectively.

Each voxel in both the low- and high-energy image contains information of the lesion and the normal tissue. Because two images are acquired with different energies, the iodine attenuation from the lesion can be unraveled by manipulating the two equations above [13–16].

The first mathematical step is to transform the intensities using the natural logarithm. This removes the exponential function from the equations making them easier to handle:

$$\begin{aligned}\ln\left(I_{\mathrm{d}}^{\mathrm{LE}}\right) &= \ln\left(I_0^{\mathrm{LE}} \cdot \mathrm{e}^{-\left(\mu_{\mathrm{t}}^{\mathrm{LE}} \cdot t + \mu_{\mathrm{l}}^{\mathrm{LE}} \cdot T\right)}\right) \\ &= \ln\left(I_0^{\mathrm{LE}}\right) - \left(\mu_{\mathrm{t}}^{\mathrm{LE}} \cdot t + \mu_{\mathrm{l}}^{\mathrm{LE}} \cdot T\right)\end{aligned} \tag{2.2a}$$

$$\begin{aligned}\ln\left(I_{\mathrm{d}}^{\mathrm{HE}}\right) &= \ln\left(I_0^{\mathrm{HE}} \cdot \mathrm{e}^{-\left(\mu_{\mathrm{t}}^{\mathrm{HE}} \cdot t + \mu_{\mathrm{l}}^{\mathrm{HE}} \cdot T\right)}\right) \\ &= \ln\left(I_0^{\mathrm{HE}}\right) - \left(\mu_{\mathrm{t}}^{\mathrm{HE}} \cdot t + \mu_{\mathrm{l}}^{\mathrm{HE}} \cdot T\right)\end{aligned} \tag{2.2b}$$

It should be noted that the natural logarithm of the incoming intensity ($\ln\left(I_0^{\mathrm{LE}}\right)$ and $\ln\left(I_0^{\mathrm{HE}}\right)$) is a constant in Eq. (2.2b).

The second step is to subtract the logarithmic low-energy intensity from the logarithmic high-energy intensity using a specifically chosen weighting factor *w*. This *w* has a certain value and is chosen to cancel out the attenuation due to the normal tissue in the final contrast-enhanced recombined image. The subtraction can be mathematically written as:

$$\begin{aligned}\ln\left(I_{\mathrm{d}}^{\mathrm{HE}}\right) - w \cdot \ln\left(I_{\mathrm{d}}^{\mathrm{LE}}\right) &= \left[\ln\left(I_0^{\mathrm{HE}}\right) - \left(\mu_{\mathrm{t}}^{\mathrm{HE}} \cdot t + \mu_{\mathrm{l}}^{\mathrm{HE}} \cdot T\right)\right] - w \\ &\cdot \left[\ln\left(I_0^{\mathrm{LE}}\right) - \left(\mu_{\mathrm{t}}^{\mathrm{LE}} \cdot t + \mu_{\mathrm{l}}^{\mathrm{LE}} \cdot T\right)\right]\end{aligned} \tag{2.3}$$

This equation can be reshuffled to group the constant values, the tissue thickness (*t*)-dependent terms, and lesion thickness (*T*)-dependent terms together. This results in:

$$\begin{aligned}\ln\left(I_{\mathrm{d}}^{\mathrm{HE}}\right) - w \cdot \ln\left(I_{\mathrm{d}}^{\mathrm{LE}}\right) &= \left[\ln\left(I_0^{\mathrm{HE}}\right) - w \cdot \ln\left(I_0^{\mathrm{LE}}\right)\right] - \left[\mu_{\mathrm{t}}^{\mathrm{HE}} - w \cdot \mu_{\mathrm{t}}^{\mathrm{LE}}\right] \cdot t \\ &- \left[\mu_{\mathrm{l}}^{\mathrm{HE}} - w \cdot \mu_{\mathrm{l}}^{\mathrm{LE}}\right] \cdot T\end{aligned} \tag{2.4}$$

In this equation, there is only one term that contains the thickness of the normal tissue *t* and one term containing the thickness of the lesion *T*. Again, the natural logarithm of the incoming intensities is a constant value, indicated by *C* in the next equations.

The third step is to choose the weighting factor *w* such that the term containing the tissue thickness *t* becomes zero. This can be achieved by making $\left[\mu_{\mathrm{t}}^{\mathrm{HE}} - w \cdot \mu_{\mathrm{t}}^{\mathrm{LE}}\right]$ to become zero, namely, by taking $w = \mu_{\mathrm{t}}^{\mathrm{HE}} / \mu_{\mathrm{t}}^{\mathrm{LE}}$. The used low- and high-energy X-ray radiation determine the value of $\mu_{\mathrm{t}}^{\mathrm{LE}}$ and $\mu_{\mathrm{t}}^{\mathrm{HE}}$ and consequently the numerical value of the weighting factor *w*.

The resulting equation shows only a dependency on the lesion thickness:

$$\ln\left(I_{\mathrm{d}}^{\mathrm{HE}}\right) - w \cdot \ln\left(I_{\mathrm{d}}^{\mathrm{LE}}\right) = C - \left[\mu_{\mathrm{l}}^{\mathrm{HE}} - w \cdot \mu_{\mathrm{l}}^{\mathrm{LE}}\right] \cdot T \tag{2.5}$$

Finally, because of the *k*-edge present in the iodine attenuation coefficient curve (Fig. 2.4), the low- and high-energy X-ray radiation can be chosen such that

$\mu_l^{LE} \sim< \mu_l^{HE}$, while the attenuation of the tissue gradually decreases: $\mu_t^{LE} > \mu_t^{HE}$ and thus $w = \mu_t^{HE} / \mu_t^{LE} < 1$. This reduces Eq. (2.5) further to:

$$\begin{aligned} \ln\left(I_d^{HE}\right) - w \cdot \ln\left(I_d^{LE}\right) &= C - \mu_l^{HE}\left[1 - w \cdot \frac{\mu_l^{LE}}{\mu_l^{HE}}\right] \cdot T \\ &\sim C - \mu_l^{HE} \cdot T \end{aligned} \tag{2.6}$$

This image that is the result of the weighted subtraction is mainly dominated by the iodine attenuation factor for the high-energy X-ray radiation.

2.3.3 Post-processing for Poly-energetic X-Ray Spectra

The above mathematics that produce the iodine contrast-enhanced image simplifies the process by assuming that a monoenergetic X-ray source is used, e.g., the low- and high-energy X-ray radiations consist of a single energy or a very narrow spectrum. In practice, a *poly-energetic* low- and high-energy spectrum is used, which contains a wider range of energies, even to the extent that the tails of the spectrum may cross the *k*-edge (Fig. 2.6). In this case, the monoenergetic approximation method may introduce errors in the recombined image, such as an increase of visible residual background structures [17].

In literature, poly-energetic solutions are presented that have practical disadvantages such as the requirement of calibrations [17, 18]. One vendor has implemented a practically feasible poly-energetic solution that in the basis expands the monoenergetic weighted subtraction with so-called second-order terms [17]:

$$T_{\text{Iodine}} \sim w_1 \cdot \ln I_d^{HE} - w_2 \cdot \ln I_d^{LE} - w_3 \cdot \left(\ln I_d^{HE}\right)^2 - w_4 \cdot \left(\ln I_d^{LE}\right) - w_5 \cdot \ln I_d^{HE} \cdot \ln I_d^{LE} \tag{2.7}$$

In this equation, T is the iodine thickness present in the voxel and I is defined as in Fig. 2.8. The constant C and the weighting factors w_1–w_5 are determined for each combination of breast thickness and low- and high-energy spectra. This is done by performing simulations using a detailed model of the imaging chain of the mammograph (tube, anode/filter material, breast, anti-scatter grid, detector). Puong et al. [17] show that this indeed leads to a significant background texture removal. Another vendor has implemented a slightly different approach using modeling based on a poly-energetic spectrum to derive the optimal weighting factor used in Eqs. (2.3–2.6).

2.3.4 Further Steps in Post-processing

Besides the calculation to produce the contrast-enhanced image, the post-processing may entail other steps, such as a correction for movement of the breast between the two acquisitions and a correction for the reduced breast thickness toward the edge of the breast. Although the time between the two acquisitions is kept short (typically 0.6–20 s) and the breast remains compressed during the whole CEM acquisition,

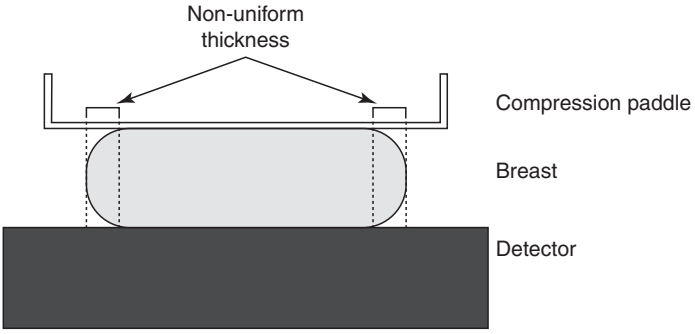

Fig. 2.9 During compression the breast has a uniform thickness, except at the edges as is illustrated here

there may be some movement which may lead to ripple artifacts if unaccounted for [19]. To circumvent this, the low- and high-energy image can be co-registered before further post-processing takes place.

The post-processing algorithm assumes the breast thickness to be uniform which is the case when the breast is compressed except for the edges (see Fig. 2.9). As a result, the total attenuation at the edges is lower which may lead to errors in the calculation of the iodine content in those voxels. The post-processing incorporates corrections for this [17, 20].

2.3.5 Interpretation of Gray Values in Iodine Contrast-Enhanced Image

For each voxel in the image, the calculated iodine contrast enhancement is displayed as a gray value. Since CEM is a two-dimensional technique, each voxel is the result of a projection along a line through the breast (Fig. 2.8) and only the cumulative iodine content along that line can be determined. Consequently, no distinction can be made between a thick lesion with a low iodine concentration (low attenuation μ) and a thin lesion with a high iodine concentration (high attenuation μ) (Fig. 2.10). Therefore, it should be realized that the gray values never represent absolute iodine concentrations (mg/ml or mg/cm^3) but represent the so-called iodine mass thickness (IMT, mg/cm^2) [21, 22]. IMT is a cumulative value of the iodine present in the projection line of a voxel.

2.4 Commercial Implementation

At the time of writing this chapter, three vendors have four commercially available CEM systems. CEM is integrated in their FFDM units that are adapted to allow a rapidly switch to the HE spectrum, read out two acquisitions in a short time period, and perform the necessary post-processing. For the patient, CEM acquisition is

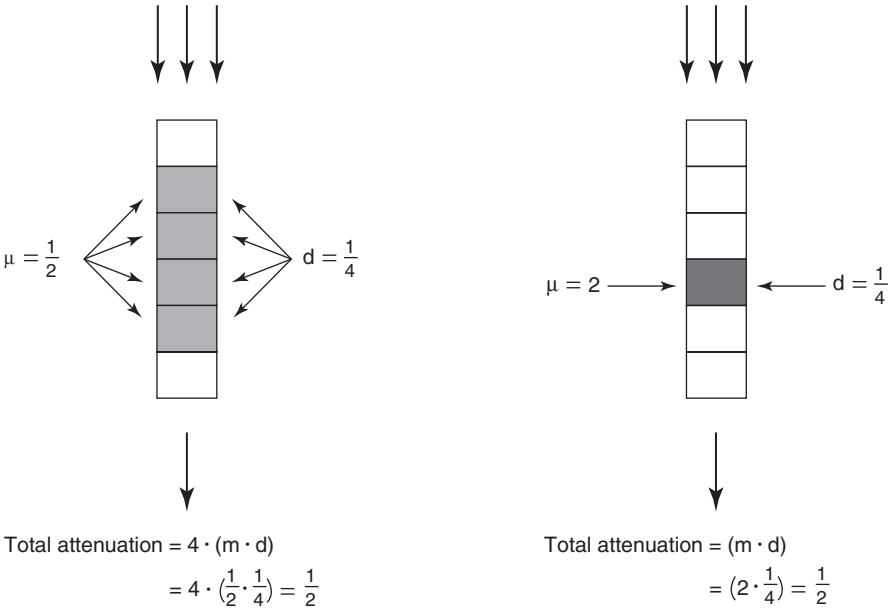

Fig. 2.10 As CEM is a 2D projection technique only the cummulative iodine content along the projection line can be determined. A low concentration but thicker lesion can result in the same grey value as a high concentration thinner lesion

similar to a regular FFDM acquisition: the machine has the same appearance and the same method of compression and positioning, and there is no additional movement of the X-ray tube such as in digital breast tomosynthesis. The main difference during the acquisition is that the total acquisition time of the CEM is a few seconds longer than a FFDM acquisition.

As indicated in Sect. 2.2.3, the high-energy X-ray spectrum needs to be above the iodine *k*-edge and in addition as narrow or monoenergetic as possible. This can be achieved by choosing a higher tube voltage and inserting a filter that absorbs the low-energy photons thoroughly. By choosing a thicker filter, the spectrum becomes narrower, but to maintain enough X-ray intensity for imaging the X-ray, tube output needs to increase. In this respect, vendors have made a trade-off. The high-energy spectrum is generated by using the same anode material as in the low-energy acquisition. For one vendor there are two available anode materials for the low-energy acquisition, and one is chosen based on breast thickness and composition. The same anode material is also always used for the high-energy acquisition. The filter material and tube voltage are switched after the low-energy acquisition to obtain the high-energy spectrum for the second acquisition. The typical switching time ranges from 0.6 to 20 s depending on the vendor. The total acquisition time depends on breast thickness and composition and ranges from 2 to 22 s for the different vendors. Table 2.1 shows the technical specification of the low- and high-energy spectra used in the commercial systems.

Table 2.1 Settings for the low-energy and high-energy CEM acquisition for the four currently commercially available CEM systems

	GE Healthcare		Hologic	Siemens Healthineers
	Senographe Essential SenoBright	Senographe Pristina SenoBright HD	Selenia Dimensions/ 3Dimensions I-View	MAMMOMAT Revelation TiCEM
Low-energy acquisition				
Anode/filter material	Mo/Mo; Mo/Rh; Rh/Rh	Mo/Mo; Rh/Ag	W/Rh; W/Ag	W/Rh
Thickness filter (mm)	Mo: 0.03; Rh 0.025	Mo: 0.03; Ag 0.03	0.050	0.050
Tube voltage range (kV)	26–31	Mo/Mo: 26 Rh/Ag: 34[a]	25–33	28–34
High-energy acquisition				
Anode/filter material	Mo/Al + Cu; Rh/Al + Cu	Rh/Cu	W/Cu	W/Ti
Thickness filter (mm)	Al: 0.3; Cu: 0.3	0.25	0.3	1.0
kV range	45–49	49[a]	45–49	49
Total acquisition time (s)	2.5–7.5	2.5–7.5	<2	<22

Source: Personal communication with J. Korporaal, Siemens Healthineers; S. Muller, GE Healthcare; A. Smith, Hologic; May–Oct 2018
Mo molybdenum, *Rh* rhodium, *Ag* silver; *W* tungsten, *Cu* copper, *Ti* titanium
[a]When the automated exposure control is not used, a larger kV range is possible: LE 22–50 kVp; HE 40–49 kV

2.5 Breast Dose: Mean Glandular Dose Calculation

During a mammographic acquisition, the breast is exposed to radiation which is partly absorbed. As the glandular tissue is the most radiosensitive tissue present in the breast, the mean dose to the glandular tissue or mean glandular dose (MGD) is recommended as a dosimetric quantity [23]. The MGD can be related to the carcinogenic risk. The MGD cannot be measured directly; however, it can be calculated from the incident dose or air kerma at the top surface of the compressed breast using appropriate conversion factors [23, 24]. The conversion factors are based on Monte Carlo computer simulations and are tabulated for a range of breast thicknesses, glandularity, and, initially, low-energy FFDM spectra [25–27]. To accommodate MGD calculation for high-energy spectra in CEM, later on also conversion factors were published for spectra in this energy range [28].

CEM acquires a high-energy acquisition in addition to the low-energy acquisition that is equal to an FFDM acquisition [9–11]. Therefore, it is to be expected that the MGD for CEM is higher compared to FFDM. Only a few studies have been reported regarding the MGD for a commercially implemented CEM. The reported mean MGD values for unilateral single-view CEM acquisition are in the range of 2.49–3.0 mGy for a mean compressed breast thickness in the study population of

56–63 mm [29–32] (Table 2.2). Although the reported MGD values for CEM are very similar, the percentage increase with respect to FFDM varies considerably, ranging from 42% to 81%, due to variations in the reported MGD values for FFDM. It is therefore important also to consider both the CEM and FFDM dose values and not only the percentage increase. Both Badr et al. and Jeukens et al. found that the high-energy acquisition contributes 24–25% to the total MGD of a CEM acquisition. All reported doses are below the acceptable limits set by regulatory institutions [24, 33].

The MGD can be used to relate the radiation exposure to risk of health detriment being the incidence of (non-)fatal cancer. To this extent age-dependent lifetime attributable risk (LAR) factors are published by the Biological Effects of Ionizing Radiation VII committee [34]. For a unilateral, single-view CEM acquisition having an MGD of 2.8 mGy, the LAR for cancer incidence is 2 (age = 40 years), 0.4 (age = 60 years), and <0.1 (age = 80 years) cases out of 100,000 persons. The LAR values for cancer mortality are about 2–3 times lower. From these data one can conclude that CEM exposure poses only a small additional risk compared to the lifetime risk for breast cancer incidence and mortality of 12,000 and 3000 cases per 100,000 women, respectively [34].

Table 2.2 Comparison of MGD for unilateral single-view CEM and FFDM acquisitions reported in literature

	CEM			FFDM		
	Study population (images/patients)	MGD (mean ± SD[a]) [mGy]	Mean (±SD[a]) compressed breast thickness (mm)	Study population (images/patients)	MGD (mean ± SD[a]) [mGy]	Mean (±SD[a]) compressed breast thickness (mm)
Badr et al. [29] (system 1)	391/104	2.65 ± 0.78	56	360/104	1.72 ± 0.96	57
Jeukens et al. [30] (system 1)	193/47	2.80 ± 0.88	58 ± 14	2577/715	1.55 ± 0.48	56 ± 14
James et al. [31] (system 2)	173/173	3.0 ± 1.1	63	6214/6214	1.8 ± 0.9	47[b]
Phillips et al. [32] (systems 1 and 2)	180/45	2.49[c]	56	180/45	1.40 (system 1)[c] 2.16 (system 2)[c]	56

System 1 indicates the GE Healthcare Senographe Essential, system 2 the Hologic Selenia Dimensions

[a]Not all studies report the SD

[b]James et al. report in addition that the CEM MGD is 42% higher than the FFDM MGD for a 63 mm compressed breast thickness

[c]The study reports MGD values for CEM of system 1 and for FFDM for systems 1 and 2

References

1. Alvarez RE, Macovski A. Energy-selective reconstructions in X-ray computerized tomography. Phys Med Biol. 1976;21(5):733–44. PMID: 967922.
2. Brody WR, Butt G, Hall A, Macovski A. A method for selective tissue and bone visualization using dual energy scanned projection radiography. Med Phys. 1981;8(3):353–7. PMID: 7033756.
3. Lehmann LA, Alvarez RE, Macovski A, Brody WR, Pelc NJ, Riederer SJ, Hall AL. Generalized image combinations in dual KVP digital radiography. Med Phys. 1981;8(5):659–67. PMID: 7290019.
4. Johns PC, Drost DJ, Yaffe MJ, Fenster A. Dual-energy mammography: initial experimental results. Med Phys. 1985;12(3):297–304. PMID: 4010634.
5. Johns PC, Yaffe MJ. X-ray characterisation of normal and neoplastic breast tissues. Phys Med Biol. 1987;32(6):675–95. PMID: 3039542.
6. Lalji U, Lobbes M. Contrast-enhanced dual-energy mammography: a promising new imaging tool in breast cancer detection. Womens Health. 2014;10(3):289–98. PMID: 24956295.
7. ICRU. Tissue substitutes in radiation dosimetry and measurement, report 44 of the international commission on radiation units and measurements. Bethesda, MD: ICRU; 1989. https://physics.nist.gov/PhysRefData/XrayMassCoef/tab4.html. Accessed 13 Sept 2018.
8. Dromain C, Canale S, Saab-Puong S, Carton AK, Muller S, Fallenberg EM. Optimization of contrast-enhanced spectral mammography depending on clinical indication. J Med Imaging (Bellingham). 2014;1(3):033506. PMID: 26158058.
9. Fallenberg EM, Dromain C, Diekmann F, Renz DM, Amer H, Ingold-Heppner B, Neumann AU, Winzer KJ, Bick U, Hamm B, Engelken F. Contrast-enhanced spectral mammography: does mammography provide additional clinical benefits, or can some radiation exposure be avoided? Breast Cancer Res Treat. 2014;146(2):371–81. PMID: 24986697.
10. Francescone MA, Jochelson MS, Dershaw DD, Sung JS, Hughes MC, Zheng J, Moskowitz C, Morris EA. Low energy mammogram obtained in contrast-enhanced digital mammography (CEDM) is comparable to routine full-field digital mammography (FFDM). Eur J Radiol. 2014;83(8):1350–5. PMID: 24932846.
11. Lalji UC, Jeukens CR, Houben I, Nelemans PJ, van Engen RE, van Wylick E, Beets-Tan RG, Wildberger JE, Paulis LE, Lobbes MB. Evaluation of low-energy contrast-enhanced spectral mammography images by comparing them to full-field digital mammography using EUREF image quality criteria. Eur Radiol. 2015;25(10):2813–20. PMID: 25813015.
12. Lobbes MB, Smidt ML, Houwers J, Tjan-Heijnen VC, Wildberger JE. Contrast enhanced mammography: techniques, current results, and potential indications. Clin Radiol. 2013;68(9):935–44. PMID: 23790689.
13. Richard S, Siewerdsen JH. Cascaded systems analysis of noise reduction algorithms in dual-energy imaging. Med Phys. 2008;35(2):586–601. PMID: 18383680.
14. Markay MK. Physics of mammographic imaging. Boca Raton, FL: CRC Press; 2013. ISBN: 978-1–4398-7544-5.
15. Hill ML, Mainprize JG, Carton AK, Saab-Puong S, Iordache R, Muller S, Jong RA, Dromain C, Yaffe MJ. Anatomical noise in contrast-enhanced digital mammography. Part II. Dual-energy imaging. Med Phys. 2013;40(8):081907. PMID: 23927321.
16. Hu YH, Scaduto DA, Zhao W. Optimization of contrast-enhanced breast imaging: analysis using a cascaded linear system model. Med Phys. 2017;44(1):43–56. PMID: 28044312.
17. Puong S, Bouchevreau X, Paoureaux F, Iordache R, Muller S. Dual-energy contrast enhanced digital mammography using a new approach for breast tissue canceling. 2007 Medical imaging proceedings of SPIE, vol 6510 65102H/Proceedings volume 6510, medical imaging 2007: physics of medical imaging; 65102H. 2007. https://doi.org/10.1117/12.710133.
18. Contillo A, Di Domenico G, Cardarelli P, Gambaccini M, Taibi A. A novel approach to background subtraction in contrast-enhanced dual-energy digital mammography with commercially

available mammography devices: polychromaticity correction. Med Phys. 2015;42(11):6641–50. PMID: 26520754
19. Yagil Y, Shalmon A, Rundstein A, Servadio Y, Halshtok O, Gotlieb M, Sklair-Levy M. Challenges in contrast-enhanced spectral mammography interpretation: artefacts lexicon. Clin Radiol. 2016;71(5):450–7. PMID: 26897335
20. Korporaal JG, Hörnig MD, Mertelmeier T, Hebecker A. Titanium contrast-enhanced mammography (TiCEM). White paper. Erlangen: Siemens Healthineers; 2018.
21. Hwang YS, Cheung YC, Lin YY, Hsu HL, Tsai HY. Susceptibility of iodine concentration map of dual-energy contrast-enhanced digital mammography for quantitative and tumor enhancement assessment. Acta Radiol. 2018;59(8):893–901. PMID: 29117707.
22. Lobbes MBI, Mulder HKP, Rousch M, Backes WH, Wildberger JE, Jeukens CRLPN. Quantification of enhancement in contrast-enhanced spectral mammography using a custom-made quantifier tool (I-STRIP): a proof-of-concept study. Eur J Radiol. 2018;106:114–21. PMID: 30150032.
23. Dance DR. Monte Carlo calculation of conversion factors for the estimation of mean glandular breast dose. Phys Med Biol. 1990;35(9):1211–9. PMID: 2236205.
24. European Communities. European guidelines for quality assurance in breast cancer screening and diagnosis. 4th ed. Luxembourg: Office for Official Publications of the European Communities; 2006.
25. Wu X, Gingold EL, Barnes GT, Tucker DM. Normalized average glandular dose in molybdenum target-rhodium filter and rhodium target-rhodium filter mammography. Radiology. 1994;193(1):83–9. PMID: 8090926.
26. Boone JM. Glandular breast dose for monoenergetic and high-energy X-ray beams: Monte Carlo assessment. Radiology. 1999;213(1):23–37. PMID: 10540637.
27. Dance DR, Skinner CL, Young KC, Beckett JR, Kotre CJ. Additional factors for the estimation of mean glandular breast dose using the UK mammography dosimetry protocol. Phys Med Biol. 2000;45(11):3225–40. PMID: 11098900.
28. Dance DR, Young KC. Estimation of mean glandular dose for contrast enhanced digital mammography: factors for use with the UK, European and IAEA breast dosimetry protocols. Phys Med Biol. 2014;59(9):2127–37. PMID: 24699200.
29. Badr S, Laurent N, Régis C, Boulanger L, Lemaille S, Poncelet E. Dual-energy contrast-enhanced digital mammography in routine clinical practice in 2013. Diagn Interv Imaging. 2014;95(3):245–58. PMID: 24238816.
30. Jeukens CR, Lalji UC, Meijer E, Bakija B, Theunissen R, Wildberger JE, Lobbes MB. Radiation exposure of contrast-enhanced spectral mammography compared with full-field digital mammography. Investig Radiol. 2014;49(10):659–65. PMID: 24872005.
31. James JR, Pavlicek W, Hanson JA, Boltz TF, Patel BK. Breast radiation dose with CESM compared with 2D FFDM and 3D tomosynthesis mammography. AJR Am J Roentgenol. 2017;208(2):362–72. PMID: 28112559.
32. Phillips J, Mihai G, Hassonjee SE, Raj SD, Palmer MR, Brook A, Zhang D. Comparative dose of contrast-enhanced spectral mammography (CESM), digital mammography, and digital breast tomosynthesis. AJR. 2018;211:839–46.
33. Food and Drug Administration. Mammography quality standards act regulations. https://www.fda.gov/Radiation-EmittingProducts/MammographyQualityStandardsActandProgram/Regulations/ucm110906.htm#s90012. Accessed 13 Sept 2018.
34. National Research Council. Health risks from exposure to low levels of ionizing radiation: BEIR VII phase 2. Washington, DC: National Academic Press; 2006.